ADVANCED ENERGY MATERIALS
www.advenergymat.de

Exploring the Interface of Skin-Layered Titanium Fibers for Electrochemical Water Splitting

*Chang Liu, Meital Shviro, Aldo S. Gago, Sarah F. Zaccarine, Guido Bender, Pawel Gazdzicki, Tobias Morawietz, Indro Biswas, Marcin Rasinski, Andreas Everwand, Roland Schierholz, Jason Pfeilsticker, Martin Müller, Pietro P. Lopes, Rüdiger-A. Eichel, Bryan Pivovar, Svitlana Pylypenko, K. Andreas Friedrich, Werner Lehnert, and Marcelo Carmo**

Water electrolysis is the key to a decarbonized energy system, as it enables the conversion and storage of renewably generated intermittent electricity in the form of hydrogen. However, reliability challenges arising from titanium-based porous transport layers (PTLs) have hitherto restricted the deployment of next-generation water-splitting devices. Here, it is shown for the first time how PTLs can be adapted so that their interface remains well protected and resistant to corrosion across ≈4000 h under real electrolysis conditions. It is also demonstrated that the malfunctioning of unprotected PTLs is a result triggered by additional fatal degradation mechanisms over the anodic catalyst layer beyond the impacts expected from iridium oxide stability. Now, superior durability and efficiency in water electrolyzers can be achieved over extended periods of operation with less-expensive PTLs with proper protection, which can be explained by the detailed reconstruction of the interface between the different elements, materials, layers, and components presented in this work.

1. Introduction

Society is rapidly progressing toward the widespread use of sustainable energy conversion devices such as polymer electrolyte membrane (PEM) water electrolyzers for power-to-gas applications.[1,2] These electrochemical systems are deployed to secure resilient power management in regions with access to renewable energy sources that are, by their nature, intermittent.[3–6] Limitations to the durability of components used in water electrolyzers and overall process efficiency are major obstacles to the deployment of these devices at scale. Therefore, significant development is needed in order for energy storage applications to achieve rapid and significant market penetration.

C. Liu, Dr. M. Shviro, A. Everwand, Dr. M. Müller, Prof. W. Lehnert, Prof. M. Carmo
Forschungszentrum Jülich GmbH
Institute of Energy and Climate Research (IEK-14): Electrochemical Process Engineering
52425 Jülich, Germany
E-mail: m.carmo@fz-juelich.de

Dr. A. S. Gago, Dr. P. Gazdzicki, T. Morawietz, Dr. I. Biswas, Prof. K. A. Friedrich
Institute of Engineering Thermodynamics
German Aerospace Center (DLR)
Pfaffenwaldring 38–40, 70569 Stuttgart, Germany

S. F. Zaccarine, Prof. S. Pylypenko
Department of Chemistry
Colorado School of Mines
Golden, CO 80401, USA

Dr. G. Bender, J. Pfeilsticker, Dr. B. Pivovar, Prof. S. Pylypenko
National Renewable Energy Laboratory
Golden, CO 80401, USA

The ORCID identification number(s) for the author(s) of this article can be found under https://doi.org/10.1002/aenm.202002926.

DOI: 10.1002/aenm.202002926

T. Morawietz, Prof. K. A. Friedrich
Institute for Building Energetics
Thermotechnology and Energy Storage (IGTE)
University of Stuttgart
Pfaffenwaldring 31, 70569 Stuttgart, Germany

Dr. M. Rasinski
Forschungszentrum Jülich GmbH
Institute of Energy and Climate Research
Plasma Physics (IEK-4)
52425 Jülich, Germany

Dr. R. Schierholz, Prof. R.-A. Eichel
Forschungszentrum Jülich GmbH
Institute of Energy and Climate Research (IEK-9): Fundamental Electrochemistry
52425 Jülich, Germany

Dr. P. P. Lopes
Materials Science Division
Argonne National Laboratory
Lemont, IL 60439, USA

Prof. R.-A. Eichel
Rheinisch-Westfälische Technische Hochschule Aachen
Institute of Physical Chemistry
52056 Aachen, Germany

Prof. W. Lehnert
Modeling in Electrochemical Process Engineering
RWTH Aachen University
52056 Aachen, Germany

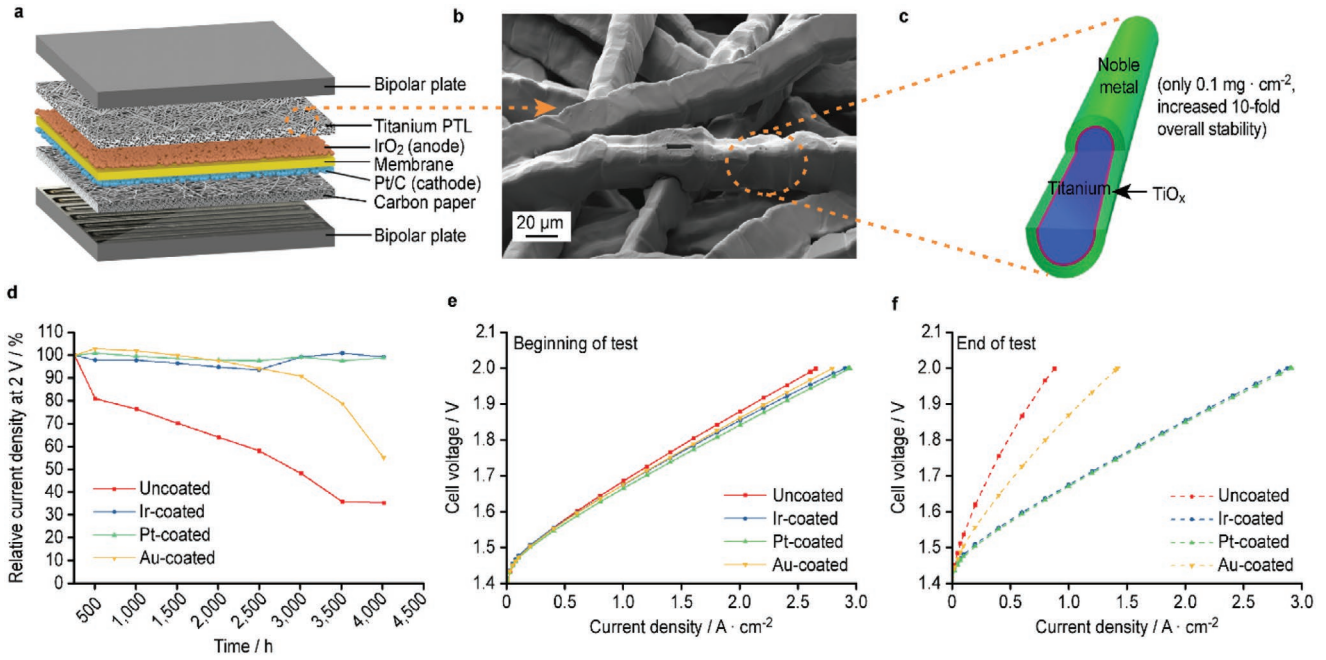

Figure 1. Principle of skin-layered titanium fibers and electrochemical performance. a) Schematic illustration of the key components inside a water-splitting device (PEM electrolyzer). b) Focused ion beam-scanning electron microscope (FIB-SEM) image of an Ir-coated PTL. c) Illustration of a cross section of a single titanium fiber coated with Ir or other noble metals such as Pt or Au (green). The coating ultimately inhibits the further growth of the oxide layer (red) compared to uncoated titanium fibers (blue), limiting increases in the cell resistance over time. d) Relative current density at 2 V (the average value of current density between 200 and 250 h (conditioning) was determined to be 100%). e) Polarization curves of all PEM electrolyzer single cells assembled with uncoated, Ir-coated, Pt-coated, and Au-coated PTLs prior to 4000 h of operation. f) Polarization curves of all PEM electrolyzer single cells assembled with uncoated, Ir-coated, Pt-coated, and Au-coated PTLs after 4000 h of operation.

When dealing with electrochemical devices comprised of a series of functional layers such as those found in batteries,[7–9] fuel cells,[10–12] solar cells,[13,14] electrolyzers,[15–17] and supercapacitors,[18–20] a fundamental challenge still exists with regard to properly stabilizing the interfaces generated between the assembled elements, materials, and components. Herein, for the first time, we locally visualize the nanoscopic changes and interplay between the materials in a PEM electrolyzer with a focus on one of the most important interfaces, that between the porous transport layers (PTLs) and electrodes. Our results demonstrate the dramatic impact that an optimized PTL/electrode interface can have on the performance and durability of a water-splitting cell.

Highly corrosion-resistant materials such as titanium fibers are typically used to construct cell/stack components in PEM water electrolyzers, the main components of which are presented in **Figure 1**a. The anode PTL is a key component and works to transport water to the anode, conduct electrons, and remove the oxygen that is produced. However, the detrimental passivation of titanium-based components, which occurs under realistic cell-operating conditions, is a major issue, limiting its application at scale. Due to harsh acidic conditions, high cell overpotentials, and oxygen evolution, the oxidation state of titanium (Ti^0) changes over time, leading to the significant degradation of titanium-based components on the anode side.[6,21–24] At present, noble metals such as gold and platinum are used as protective coatings on PTLs and bipolar plates (BPs).[22–29] We have previously reported that cells assembled with platinum-coated PTLs show substantially reduced degradation rates compared to cells with uncoated PTLs.[23,24] More recently, we have shown a simple and scalable method to protect titanium PTLs by sputtering thin layers of iridium, which effectively decreased the contact resistance and significantly improved cell performance.[21] Nevertheless, it is of crucial importance to understand the interplay between components and materials that affect efficiency and durability and elucidate how these coatings behave under realistic cell-operating conditions, especially after long-term operation. Changes in physical–chemical conditions such as morphology, oxidation state, degree of corrosion, and dissolution and the resulting impacts on electrical conductivity that lead to superior durability concerns are of particular interest. Establishing such correlations will guide future design strategies for novel coatings that can allow the use of less-expensive materials and components for optimal cell-operating conditions.

In this study, stable cell performance profiles were obtained after ≈4000 h with titanium PTLs that contained a skin surface layer composed of iridium or platinum. For the first time, we show herein that the iridium skin over the titanium fibers was preserved in its metallic oxidation state and remained remarkably stable throughout the entire test. In contrast, our results indicate that uncoated or poorly coated PTLs trigger severe degradation of the catalyst layer (CL), which suggests that catalyst layer degradation can be caused by secondary components used in the cell. Skin-layered fibers could, therefore, enable the

Prof. M. Carmo
Mechanical and Materials Engineering
Queen's University
Kingston, Ontario K7L 3N6, Canada

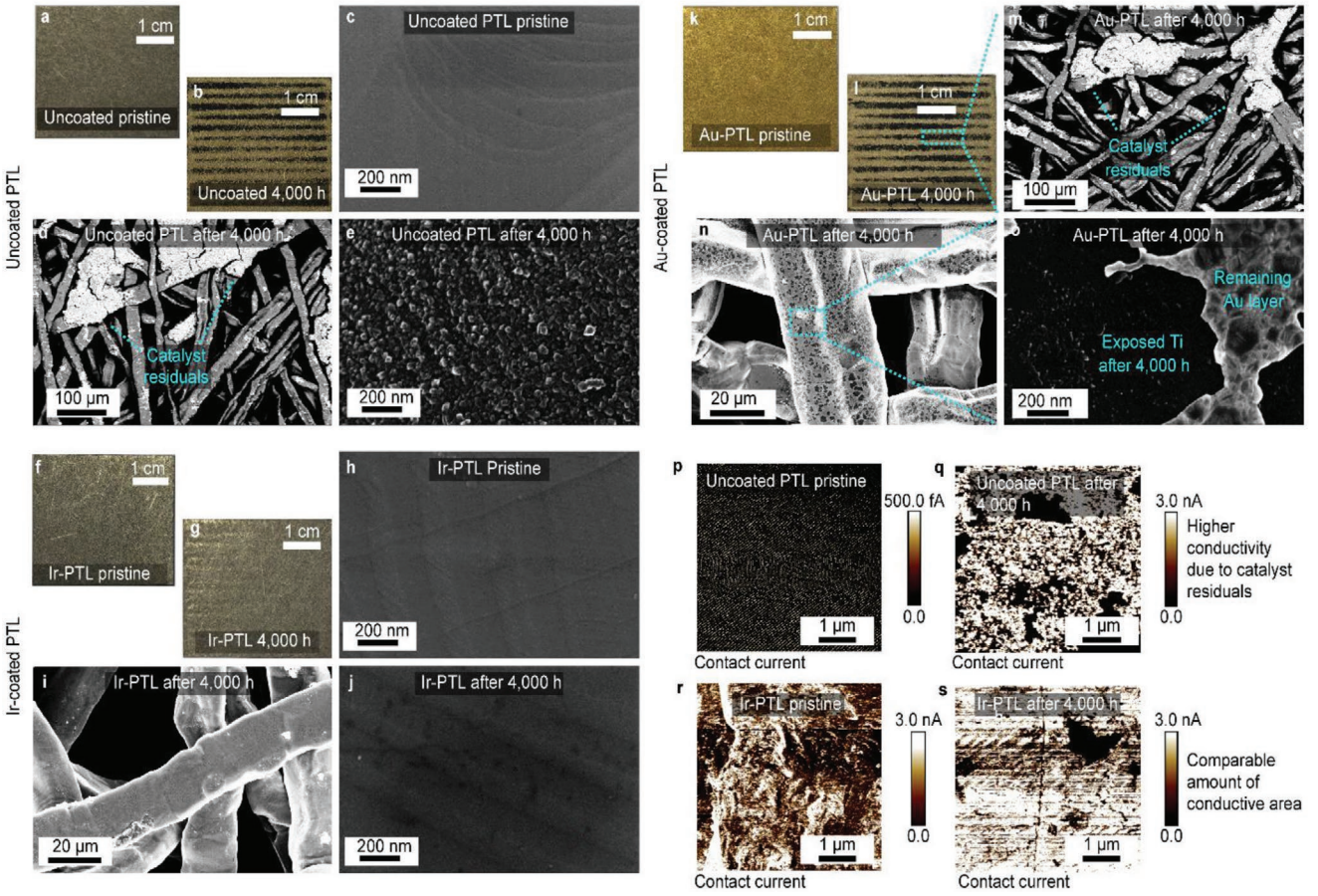

Figure 2. Optical, SEM, and AFM images of PTLs before and after 4000 h operation. a,b) Optical images of uncoated PTL. c–e) SEM images of an uncoated PTL. f,g) Optical images of Ir-coated PTLs. h–j) SEM images of Ir-coated PTL. k,l) Optical images of Au-coated PTL. m–o) SEM images of Au-coated PTL. p,q) AFM conductivity measurement of uncoated PTL. r,s) AFM conductivity measurement of an Ir-coated PTL.

long-term usage of PEM water electrolyzers with low degradation and cost. From a broader perspective, the results of this work represent a milestone in the investigation of interfacial phenomena and are applicable to many other energy storage and conversion devices.

2. Results and Discussion

2.1. Analysis of Electrochemical Performance and Durability

The focused ion beam (FIB) scanning electron microscopy (SEM) image of an Ir-coated titanium PTL displayed in Figure 1b highlights the 3D structure of the PTL, with a fiber diameter of around 20 µm. Optimized cell compression is essential in order to provide sufficient electrical contact between the electrode and PTL. However, as is illustrated in Figure 1c, off-the-shelf titanium PTLs already possess a TiO_x surface-passivation layer (red), as it was exposed to ambient air during handling, storage, and shipping.[30]

Figure 1d shows the relative current density over the 4000 h period for all four cells assembled with Ir-coated, Pt-coated, Au-coated, and uncoated PTLs. All cells were continuously operated at a constant voltage of 2 V, at 80 °C, and with ultrapure deionized (DI) water. The cells assembled with Ir-coated and Pt-coated PTLs did not show any significant decay (less than 1%) in performance beyond 4000 h. In contrast, the cells assembled with Au-coated and uncoated PTLs showed, respectively, a 35% and a 55% current density decrease after the same time period. The current density versus operating time is discussed in more detail in Note S1 (Supporting Information). The polarization curves recorded at the beginning and end of the test yielded results that are in agreement with the long-term profiles, as is shown in Figure 1e,f. Ir-coated and Pt-coated PTLs displayed identical cell performances after 4000 h of operation. Although Pt has been more widely used in industrial applications, our results demonstrate the vastly superior protection of our coating method compared to any alternative methods reported hitherto, which often leave portions of the Ti-based PTLs exposed. Decreased performance was observed for the Au-coated and uncoated PTLs. When comparing the high-frequency resistances (HFRs) for all samples, the HFR of Au-coated and uncoated PTLs increased from 0.168 to 0.292 Ω cm^2, and from 0.179 to 0.347 Ω cm^2 at 1.9 A cm^{-2}, respectively (Figure S2, Supporting Information), while values for Ir-coated and Pt-coated PTLs remained constant for the duration of the experiments. In addition, the interfacial contact resistance results correspond well go the results obtained from the polarization curves and durability profiles (Figure S3, Supporting Information).

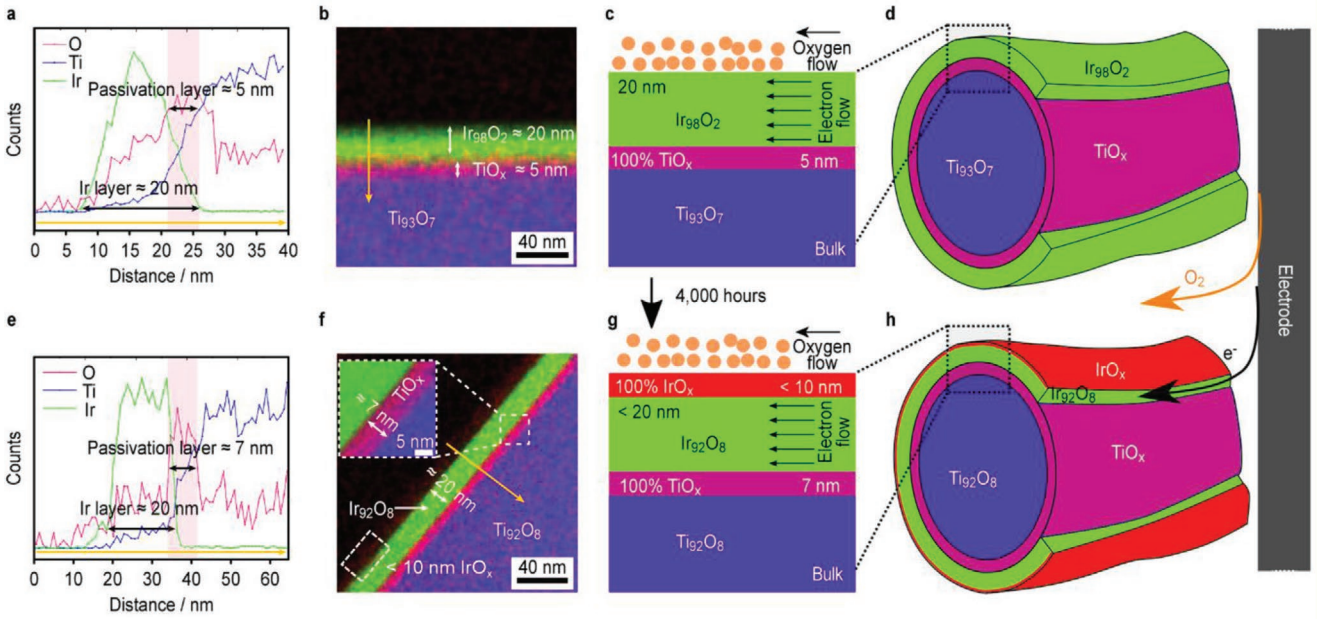

Figure 3. EDX composition analysis of the Ir-coated PTL. a,e) Line-scanning profile after FIB cross section of Ir-coated PTLs: a) pristine Ir-coated PTL and e) Ir-coated PTL after 4000 h of operation. b,f) Elemental distribution of Ir (green), O (red), and Ti (blue) in EDX composition maps: b) pristine Ir-coated PTL and f) Ir-coated PTL after 4000 h of operation. c,g) Corresponding schematics of elemental distribution of Ir, O, and Ti in EDX composition maps: c) pristine and g) after 4000 h of operation. d,h) Schematics of one Ir-coated Ti fiber: d) pristine and h) after 4000 h of operation.

2.2. Analysis of the Porous Transport Layer Structure and Morphology

PTLs used in commercial electrolyzers are typically coated with platinum or gold,[22–24,31] and loadings of their protective coatings are estimated to be around 1 mg_{metal} cm^{-2}.[32,33] We recently demonstrated a facile approach to applying 20 nm thick iridium layers to PTLs using a simple sputter process.[21] The total amount of iridium added was 0.1 mg_{Ir} cm^{-2}, which is 20 times less compared to what is usually present in an anode catalyst layer,[4] and a 10 times reduction in noble metal loading compared to the Au or Pt protective layers typically used in contemporary commercial electrolyzers.[32,33] **Figure 2**a,b shows images of the surface of an uncoated PTL prior to and after 4000 h of operation. Compared to a pristine-uncoated PTL (Figure 2c), the SEM image of the aged uncoated sample (Figure 2e) shows corrosion-yielding structures at the 30 nm scale. On the side of the PTL that faces the electrode, catalyst residual deposits can be found (Figure 2b–d), indicating detachment from the catalyst layer onto the PTLs. This was also verified by the atomic force microscopy (AFM) results, which are shown in Figure 2q, indicating that the conductivity was significantly higher in the aged uncoated sample than in the pristine sample due to the catalyst residuals from the catalyst layer, which was also confirmed by topography changes (Figure S4a,c, Supporting Information). However, no catalyst residuals were observed in the aged Ir-coated PTL (Figure 2g). Furthermore, after 4000 h of operation, the Ir-coated samples showed minimal morphology changes (Figure 2h–j) and a negligible change in the conductive area (Figure 2r,s; Figure S7, Supporting Information), which indicates that the iridium coating remains stable beyond 4000 h. The Pt-coated PTL was also stable, as the SEM and AFM images show very similar results to the Ir-coated PTL (Figures S6 and S8, Supporting Information). However, for the Au-coated samples, as is shown in Figure 2n,o, strong Au delamination from the PTLs was observed on both sides of the PTL, i.e., the one facing the BP and catalyst layer. Compared to a pristine Au-coated PTL (Figure 2k; Figure S9a, Supporting Information), on the side that faces the catalyst layer, catalyst migration from the catalyst layer to the PTL fibers could also be observed after 4000 h of operation (Figure 2l,m; Figure S9e, Supporting Information), which only occurred at the interface between the catalyst layer and PTL. Moreover, Au was not detected by energy-dispersive X-ray (EDX), which indicated that Au totally dissolved on this side (Note S6, Supporting Information).

Beyond the classical observation of the morphology changes on the surface of the PTL fibers, it is much more relevant yet highly complex to monitor the interface between the PTL fiber and the protective layer. Investigating this interface will shed light on the interrelated mechanisms exerted on multiple materials and components inside the cell. Traditional lab-scale durability analysis, using liquid electrolyte and three-electrode cell setups, for instance, might not provide such a picture, as it does not include crucial parameters relating to real cell-operating conditions or contributions to the PTL by other key cell components such as the membrane, catalyst layer, ionomer, and bipolar plates. It is therefore crucial to bridge the information gained from lab-scale testing to real-world, long-term device performance by using advanced characterization methods, enabling the use of new information that can drive the development of future materials. **Figure 3** shows the first ever image of the interfacial region of an Ir-coated PTL before and after ≈4000 h of operation under real PEM electrolysis conditions. The EDX elemental composition maps and line-scanning profile after the FIB cross section indicate that prior to operation, the protective metallic iridium layer is essentially free of oxygen

(green) and has a thickness of 20 nm (Figure 3a,b). The SEM and FIB–SEM images of the Ir-coated PTL show that the surface of the titanium fiber is homogeneously covered with iridium (Figure S12a,b, Supporting Information). The native titanium oxide layer (pink) lies beneath the added Ir layer and is around 5 nm thick, which corresponds to the range reported in the literature for titanium films after oxidation when exposed to air.[30] The bulk titanium material of the fiber has an atomic ratio of 93:7 (Ti:O) prior to operation. Figure 3e–g shows that the iridium layer (green) on the fiber maintained its 20 nm thickness, indicating that the iridium layer remains intact and does not decrease in thickness. Additionally, the results reveal that the iridium layer is still mostly in its metallic state, increasing from 2 to 8 at% oxygen in terms of its composition. On its surface, however, a <10 nm thick IrO_x layer formed (Figure 3f–h, red). This suggests that the iridium layer was subjected to an initial oxidation process that most likely occurred in the first hours of operation from oxygen evolution exposure, while further oxidation of metallic iridium did not propagate to the bulk during the test. Therefore, we suggest that the phenomenon of iridium oxidation and the subsequent dissolution that occurs with iridium catalysts fully immersed in the electrolyte might not apply to iridium layers on PTLs.[34–36] Here, the iridium layer is subjected to different conditions due to its different location, outside the acidic conditions produced by the Nafion ionomer in the catalyst layer within the cell (see Figure 1). This indicates that local pH may have an important impact on the performance and stability of Ir catalytic surfaces. With the majority of bulk iridium remaining metallic, the iridium layer provides optimal conditions for ensuring both acceptable electrical conductivity and corrosion resistance.[37,38] However, the most beneficial result is that the thin layer of iridium prevented the growth of the TiO_x passivation layer (Figure 3f–h, in pink) underneath the iridium, which would have led to a significant increase in cell resistance. By contrast, the TiO_x layer for uncoated PTLs grew significantly, and the integrity of the fiber surface completely deteriorated after 4000 h in the absence of a protective layer (Figure S13, Supporting Information). These results clearly show that iridium can be used as a new class of protective material during cell operation, as it performs well under real cell conditions, which may differ from those in routine lab-scale testing.

Figure 4a–c shows an X-ray photoelectron spectroscopy (XPS) depth profile analysis of the PTLs before and after ≈4000 h of operation, and the results strongly correlate with the cross-sectional data presented in Figure 3. Samples of titanium PTLs were etched to remove atomic layers and thus access deeper areas during the continuous analysis. Focusing on the surface layers, the XPS signals have been deconvoluted (insets of Figure 4a–c) in order to quantify the oxide and metal species. Figure 4a shows the oxide-–metal ratios versus the etching time of the uncoated PTL. The metal TiO_x:Ti ratio of the pristine uncoated PTL decreased with the Ar^+ etching time, which indicates the presence of a titanium oxide passivation layer in the initial material, in agreement with the cross-sectional results previously discussed (Figure 3a,b). At the surface ($t_{etching}$ = 0 s), the TiO_x:Ti atomic ratio is 20:1. After an etching time of 110 s, the TiO_x:Ti atomic ratio drops to almost zero, i.e., the Ti-metallic peaks (Ti $2p_{1/2}$ at 460.4 eV and Ti $2p_{3/2}$ at 454.5 eV) become the more prominent species, while the oxide peaks (Ti $2p_{1/2}$ at 464 eV and Ti $2p_{3/2}$ at 458 eV[27]) vanish due to the transition from the surface oxide layer to the Ti^0 bulk and to some fraction due to oxygen depletion from ion etching. The surface TiO_x:Ti ratios of aged uncoated PTL equal to 40–60:1 in the range <100 s (Figure 4a), which demonstrates the increase in TiO_x concentration at the surface of the uncoated PTL after 4000 h of operation. In contrast, the IrO_x:Ir (Ir^0 $4f_{5/2}/4f_{7/2}$: 63.8 eV/60.7 eV; Ir^{4+} $4f_{5/2}/4f_{7/2}$: 65.4 eV/62.3 eV) and PtO_x:Pt (Pt^0 $4f_{5/2}/4f_{7/2}$: 74.0 eV/70.8 eV; Pt^{4+} $4f_{5/2}/4f_{7/2}$: 77.6 eV/74.4 eV) atomic ratios are virtually zero for Ir-coated and Pt-coated PTLs (Figure 4b,c) with exemption of a topmost IrO_x or PtO_x layer, significantly smaller than that of the uncoated PTL. After 4000 h of operation, the ratios remain almost unchanged. Additionally, the depth profiles of the oxide-to-metal ratios indicate the absence of a hidden iridium oxide or platinum layer. This is also in accordance with the EDX composition maps and line scan results, which show that the ratio of iridium to oxygen is around 92:8 after 4000 h of operation (Figure 3f).

To complement the XPS data and further elucidate difference in the interfacial region present in the Ir-coated and Pt-coated samples, time-of-flight secondary ion mass spectrometry (ToF-SIMS) depth profiles were taken and are shown for uncoated, Ir-coated, and Pt-coated samples before and after 4000 h of operation in Figure 4d–i (XPS depth profiles are provided in Figure S14 in the Supporting Information). The counts corresponding to Ti-containing ions from the Ti fibers (Ti^+ and TiO^+), Ir-containing ions from the Ir-coating (Ir^+ and $CsIrO^{2+}$), Pt-containing ions from the Pt coating (Cs_2Pt^{2+} and $CsPtO^+$), and Cs_2O^+ are plotted against the sputtering time in Figure 4. Both metallic and oxidized Ti species were observed for all pristine and aged samples, indicating that TiO_x was even present in the pristine samples, confirming the results discussed above. The pristine uncoated PTL showed an oxidized Ti layer at the surface (Figure 4d). After 4000 h of operation, the longer, less well-defined tail with a less steep slope demonstrated a thicker and rougher TiO_x layer (Figure 4g), which is also in agreement with the morphological results described previously. The pristine Ir-coated and Pt-coated PTLs (Figure 4e,f) showed a fairly similar general trend, with both of the pristine samples showing metallic Ir or Pt species on the surface of the Ti fibers, and both samples having an interfacial oxide region, as highlighted by the gray boxes in Figure 4e,f. The sharp signals of ablated $CsIrO^{2+}$ (dark green) and $CsPtO^{2+}$ (dark blue) indicated the presence of both TiO_2 and Ir or Pt at the interface between the fiber and surface coating. Interestingly, different trends were observed in the interfacial oxide regions of Ir-coated and Pt-coated PTLs after 4000 h of operation. For the Ir-coated PTL, the oxide layer width appears to increase slightly after 4000 h, indicating the growth of oxide in the interfacial region (Figure 4h). For the Pt-coated PTL, however, after 4000 h the oxide interface appears slightly sharper and shows a steeper slope compared to the pristine sample (Figure 4i).

In summary, the XPS depth profile in Figure 4a shows a TiO_2 layer in the uncoated sample, also represented in the ToF-SIMS profiles (Figure 4d–g), and from Figure 4b,c, of the coated PTLs, a surface oxide is revealed topmost on the Ir coating. From ToF-SIMS data in Figure 4e,f, and also from XPS data in Figure S14 b,c (Supporting Information), it is also clear that there is another oxide layer at the interface between coating and the Ti fiber. Although there is a minor change in the interfacial oxide layer of Ir-coated and Pt-coated PTLs after

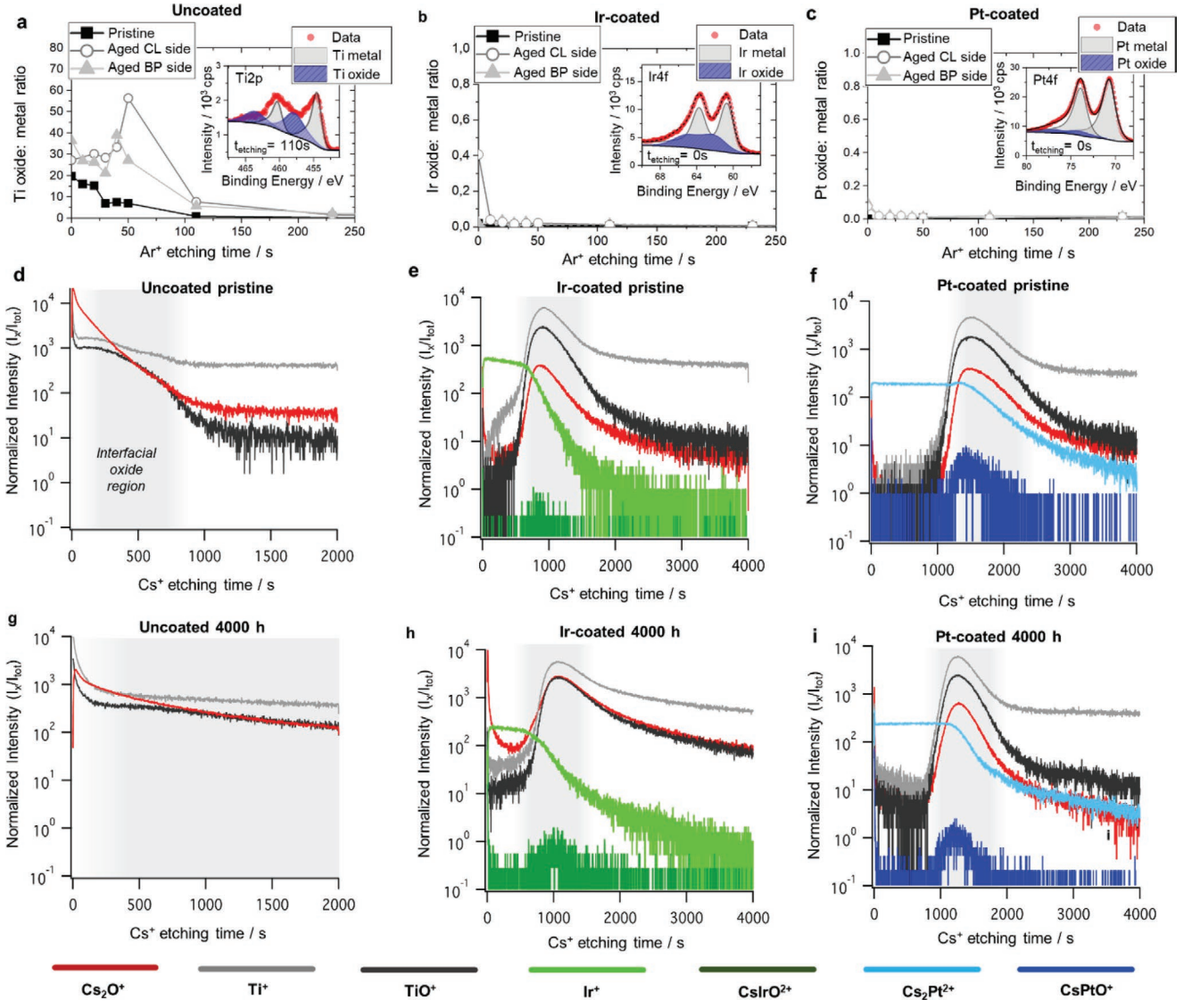

Figure 4. XPS and ToF-SIMS depth profiles of PTLs. a–c) Oxide-to-metal ratios of the pristine and aged (side that faces the catalyst layer (CL side) and side that faces the bipolar plate (BP side)) surfaces after the indicated ion etching time ($t_{etching}$) of a) uncoated, b) Ir-coated, and c) Pt-coated PTLs (depth profile). The insets provide the signal deconvolutions used to determine the oxide and metal species. d–i) ToF-SIMS profiles of PTLs: d) pristine uncoated PTL, e) pristine Ir-coated PTL, f) pristine Pt-coated PTL, g) uncoated PTL after 4000 h, h) Ir-coated PTL after 4000 h, and i) Pt-coated PTL after 4000 h. All relevant species are listed below the figure. Counts collected as a function of the sputtering time provide profiles on relevant metallic and oxide species present from the surface to the bulk of the Ti PTL fibers. Gray background boxes highlight the interfacial oxide region present between the Ti fibers and the surface or surface coating. This oxide region includes a contribution from Ti oxide and Ir or Pt oxides from the coatings. ToF-SIMS profiles measure several peaks related to the ionization of species of interest, using a Cs^+ secondary ion source. For certain species, the pure metallic ion (such as Ir^+ here) will display a stronger signal, while for others, the Cs-containing ion complex (such as Cs_2PtO^{2+}) is more intense. This depends on the electronegativity of the element and both species will reflect the same trends, with varying intensity, and so the stronger signal is chosen for clarity. The Cs_2O^+ species is representative of all oxide species present, regardless of which metal is oxidized, while the other species represent the specific features listed above.

4000 h of operation, the growth of the oxide is significantly less pronounced than in the uncoated sample, indicating that the Ir and Pt protective coatings are capable of further mitigating TiO_x layer growth in the PTL.

2.3. Analysis of the Catalyst Layer's Morphology and Stability

The results presented above indicate the impact of an increase in the interface contact resistance of a PTL component. In order to 1) exclude the possibility of having a nonfunctional catalyst-coated membrane (CCM); 2) avoid any possible error when performing the cell assembly; and 3) guarantee that all PTL samples are subjected to the same cell conditions, a special PTL was fabricated (see **Figure 5**a). For this purpose, the PTL was coated with Ir, Pt, and Au on three different sections of the same PTL, with the fourth and final section remaining uncoated. This cell was operated in the same way as the other cells, i.e., for 4000 h at 2 V and 80 °C. Figure 5a,b shows the top view on the catalyst facing the side of this PTL together with

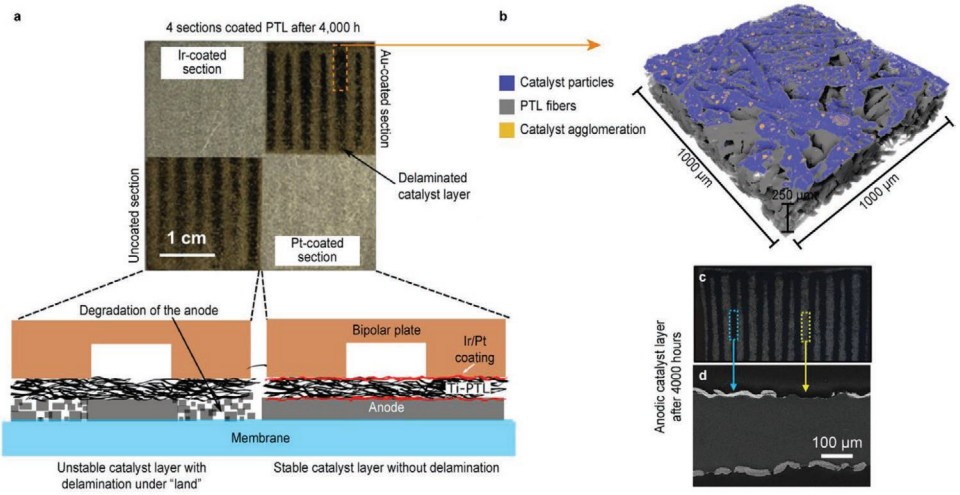

Figure 5. Delamination of catalyst layer. a) Optical image of four sections of coated PTL after 4000 h. b) X-ray CT image of Au-coated section after 4000 h (catalyst residuals are shown in blue, larger particles/catalyst agglomeration in yellow). c) Optical image of aged CCM assembled with uncoated PTL. d) Cross-sectional SEM images of aged CCM assembled with uncoated PTL.

a schematic, and an X-ray computed tomography (CT) image of the Au-coated section of this PTL, respectively. The images clearly demonstrate how the catalyst layer (blue), which was previously coated on the membrane, is transferred to the PTL. Figure 5a indicates that delamination of the catalyst layer only occurred in the uncoated and Au-coated sections during the 4000 h experiment. The CT image (Figure 5b) highlights the presence of catalyst layer particles (blue) that transferred onto the PTL material from the catalyst layer. The catalyst particles are only present on the PTL surface but did not reach the inner structure of the PTL. In addition to the transfer process, the agglomeration of catalyst particles occurred as indicated by the yellow areas of the X-ray computed tomography image. These areas consist of highly concentrated catalyst material, or, in other words, large agglomerated catalyst particles. It is apparent that the platinum group metal (PGM) coatings prevented the transfer of catalyst layer material onto the PTL surface, which only took place when the protective layer was not stable enough (Au coated) or not present.

Figure 5c,d indicates that the entire catalyst layer locally migrated to the uncoated PTL. One plausible explanation is the following. Titanium oxide has a lower thermal conductivity (4.8–11.8 W m^{-1} k^{-1}) than titanium (15.6–22.5 W m^{-1} k^{-1}) which again has a lower thermal conductivity than Pt- or Ir-coated titanium (Ir = 147 W m^{-1} k^{-1}, Pt = 71.5 W m^{-1} k^{-1}).[39] During the oxygen evolution reaction (OER), heat is generated at the active sites where the oxygen evolution takes place, and the active sites were regarded here as heat sources. The produced heat scales with the current density of the cell. The results also indicate that this effect is more pronounced at the point of contact (land vs channel) from flow fields/PTLs/catalyst layer, in other words, where there is a higher flux of electrons. Due to operation, the TiO_x passivation layer, specifically of the unprotected titanium PTL, grows and this reduces the heat flux away from the reaction sites and may cause a local temperature increase when the heat generation is larger than the heat conduction flux. As a result, hot spots are formed, which may decrease the binding characteristics of the catalyst layer, compromising its mechanical stability. This process is indicated by the delamination of the catalyst layer and its transfer from the electrode to the PTL. It is obvious that the process is suppressed when using material sets that provide a much higher thermal conductivity such as Ir-coated titanium PTLs. Nevertheless, it should be noted that the current of the cell with the uncoated PTL decreases overtime but still the generated heat might not be as well dissipated by the TiO_x compared to the Pt and Ir protective layers.

Another plausible explanation is related to the strong tendency of both Ir and Ti to form bonds with oxygen. Thus, the uncoated titanium PTL will oxidize at high potentials taking the oxygen not only from the evolved gas but also from IrO_2 catalyst as well, which is reported that it continuously forms unstable species during OER that will eventually recombine again with oxygen,[40,41] and this oxygen can be found at the interface with the uncoated titanium PTL. After the long-term operation, more and more of this unstable Ir will bond strongly with the oxygen at the interface with the uncoated titanium PTL from the passivation. It is worth noting that TiO_x is widely used in the thin-film industry as a prelayer to improve the bonding of a desired coating to a substrate. Lastly, one must not discard the tendency of polymers to adhere stronger to oxidized surfaces than metal ones,[42] which could be the case for the Nafion in the catalysts layer. Future investigation will be done to design an experiment in which we insert microtemperature sensors in the PTLs or perform adhesion tests on the catalyst layers directly deposited on the PTLs.

The high local interface resistance spots identified on our Au-coated and uncoated PTLs raised the question as to whether pinhole formation could be found on the membranes following the long-term experiment. No pinholes could be identified for all of these catalyst-coated membranes, even after 4000 h, which was measured by assessing the thermal response of hydrogen gas flowing from underneath the catalyst layer[43] (Note S10, Supporting Information).

3. Conclusion

This study presented unique approaches to improving the durability and reducing the costs of today's expensive and high PGM-containing porous transport layers used in water-splitting devices. We found that after 4000 h, stable durability profiles can be achieved when PTLs are covered with a skin layer of 0.1 mg cm^{-2} of platinum or iridium, providing for a tenfold increase in the overall stability for these devices when uncoated PTLs are used. In contrast to what was previously understood, after the formation of a <10 nm IrO_x layer on the iridium-coated PTL, bulk iridium was preserved in its metallic state, remaining remarkably stable throughout the entire test. The TiO_x layer underneath the iridium did not further passivate, in contrast to the unprotected PTL, thus preventing the cell from undergoing critical degradation. Our results also indicate that unprotected PTLs induce critical damage across the anodic catalyst layer, with a drastic deactivation observed when the uncoated PTLs were used. Here, for the first time, we were able to identify and translate degradation effects occurring at the electrode that are caused by a secondary component present in the common cell configurations of water electrolyzers. This information will aid researchers in identifying other degradation mechanisms and developing superior accelerated stress tests for these electrochemical devices. More importantly, active and stable skin-layered fibers are not only relevant to reducing the costs associated with the titanium components but also provide a pathway to extended device lifetime, offsetting the high cost of PGM-based catalysts. This study also opens new possibilities for transforming other materials, electrodes, and components where critical interface resistances using PGM or non-PGM materials play a crucial role in the long-term service life typically observed in complex devices beyond water electrolyzers, such as batteries, solar cells, and sensors.

4. Experimental Section

Cleaning and Sputtering of PTLs: A cleaning procedure was performed on all Ti-based PTL materials used in this study to remove organic substances and contaminants. The PTLs were first immersed in deionized water (Milli-Q) (18.2 MΩ cm) at 80 °C for 15 min, and then in 2-propanol and acetone in an ultrasonic bath at ambient temperature for 15 min. This procedure was followed by rinsing the PTLs twice in deionized water at 80 °C for 15 min, and finally air-drying them at ambient temperature overnight. The reasons for cleaning the PTLs at 80 °C in all the procedures were as follows: 1) removing the organic impurities and contaminates from PTL fabrication process, and this process would be faster at higher temperatures; 2) conditioning the PTL surface, exposing it to water at 80 °C so that all PTLs would have an equal starting point for cell assembly and durability start; and 3) 80 °C was chosen as it is the cell temperature.

Subsequent to cleaning the Ti-based PTLs, a plasma sputtering instrument (Quorum Q150T) was used to deposit iridium, platinum, or gold onto the PTL materials. The sputtering procedure was individually carried out for 360 s for each side of the PTLs, using a current of 30 mA, 0.7 Pa under Ar and metallic iridium, platinum, and gold targets. The loadings of the iridium, platinum, and gold were calculated by weighing the PTL materials before and after sputtering. The results are shown in **Table 1**.

Fabrication of CCMs: CCM samples were manufactured using Nafion 117 membrane as the polymer electrolyte and a combination of doctor blade and decal methods, respectively, to create and attach the electrodes. 60% Pt/C (HiSPEC 9100, Johnson & Matthey) and iridium oxide (Alfa Aesar, Premion, 99.99%) were used as the cathode and anode catalysts, respectively. Catalyst powder and ionomer solution (10% Nafion for anode and 15% Nafion for cathode) were then dispersed in appropriate mixtures of water and 2-butanol to prepare the catalyst-containing inks. The mixtures were agitated in an ultrasonic homogenizer for 5 min and then coated onto inert decal substrates with an automated bar coater (Coatmaster 509 MCI, Erichsen GmbH & Co. KG). The coated decals were dried for 30 min at room temperature. The membrane was then sandwiched between one anode and one cathode decal and hot-pressed at a temperature of 130 °C for 3 min. The decals were then removed from the sandwich following this procedure. The final catalyst layer loadings were ≈0.8 ± 3% mg_{Pt} cm^{-2} Pt/C at the cathode and ≈2.2 ± 10% mg_{Ir} cm^{-2} IrO_2 at the anode. The ratios of ionomer and catalyst were 1:4 for cathode and 1:3 for anode.

Table 1. Loading values of iridium-, platinum-, and gold-coated PTLs.

Sample	Ir-coated PTL	Pt-coated PTL	Au-coated PTL
Sputtering time [s]	360	360	360
Loading [mg cm^{-2}]	0.10	0.16	0.18

Characterization Techniques: *X-Ray CT*: The 3D microstructures of the PTLs were characterized by means of CT using a Zeiss Xradia 410 Versa X-ray.

SEM: The surface morphology of the PTLs was examined by means of SEM using a Zeiss Gemini Ultra Plus instrument.

AFM: The AFM measurements were achieved with a Multimode 8 AFM (Bruker, Karlsruhe). The sample was glued with conductive adhesive tape onto an AFM 12 mm disk with either the bipolar plate or the CCM side facing up. The sample was also connected with another conductive tape from the top close to the measurement spot in order to ensure an electrical connection. Platinum/iridium-coated AFM tips (NCHPt 42 N m^{-1}, Nanoworld) were used in tapping mode with additional recorded current that was averaged by a lock-in amplifier (PF-TUNA, Bruker). The 25 µm² measurements were recorded with 512 × 512 pixels at a scan rate of 0.5 Hz. For the conductive area evaluation, the threshold was set to 0.1 nA, while the applied voltage was 1 V.

FIB and Scanning Transmission Electron Microscope–EDX: FIB (FEI Helios NanoLab 460F1) was used to cut one titanium fiber from the PTL.[44] EDX composition maps were performed in an FEI (Thermo Fisher Scientific) Titan 80–300 electron microscope equipped with a probe corrector (CEOS) and a high-angle annular dark-field imaging detector.[45] *Z*-contrast conditions were achieved by using a probe semiangle of 25 mrad and an inner collection angle for the detector of 75 mrad.

XPS: Photoemission data were recorded using a setup with a hemispherical photoelectron analyzer (Thermo Scientific ESCALAB250) in a chamber base pressure of 5×10^{-10} mbar, using a conventional Al Kα X-ray source with an intrinsic linewidth of 0.9 eV. Depth profiles were measured by bombarding the samples with a focused Ar^+ ion beam with an acceleration voltage of 2 kV at a chamber pressure of 4×10^{-8} mbar. The ion etching yields were not calibrated for the investigated material and, hence, the depth profiles were plotted as a function of etching time only. However, in a previous paper[46] a depth calibration was performed using a Ta_2O_5/Ta reference samples with a defined thickness of the Ta_2O_5 layer, which might facilitate the comparison of these depth profiles with the data of others; the etching yield of the reference material was 0.12 nm s^{-1} at 2×10^{-8} mbar Ar partial pressure, 2 kV acceleration voltage, and 10 mA emission current.

ToF-SIMS: These measurements were performed using a ToF-SIMS 5 (ION TOF) at 30 keV with 5 µm lateral resolution with a Bi^{3+} primary ion source. The operating pressure in the analysis chamber was ≈3.1×10^{-10} mbar. Depth profiles were obtained with a 250 eV Cs^+ secondary ion source. Data were acquired using SurfaceLab 7 software. Data were plotted as a function of sputtering time; sputtering time increased from left to right and thus the sample was probed at deeper depths from left to right, respectively. For certain elements, the species itself ionizes more readily, while in other cases, species that interact with the Cs quickly ionize, depending on electronegativity, and therefore

Table 2. Parameters of characteristics and the conditions of PEM water electrolyzers.

Characteristics and conditions	Value
Membrane type	Nafion 117
Electrode area	17.64 cm^2
Anode catalyst (IrO_2)	≈2.2 ±10% mg_{Ir} cm^{-2}
Cathode catalyst (Pt/C)	≈0.8 ± 3% mg_{Pt} cm^{-2}
Anode PTL	Ir-coated PTL, Pt-coated PTL, Au-coated PTL, uncoated PTL, 4-section PTL
Cathode PTL	Toray paper (TGP-H 120)
Operating temperature	80 °C
Operating pressure	1 atm (absolute)
Water flow rate	25 mL min^{-1}

some measured species contain Cs as part of their molecular weight. Both species reflected the same trends, and the species with the higher intensity was chosen for clarity.

Single Cell Components and Assembly: Bekipor ST titanium grade 1 felts with 250 µm thicknesses and 56% porosity from Bekaert (42 × 42 mm), with and without noble metal coatings, were used as the anodic PTL. TGP-H 120 Toray paper with a 350 µm thickness was then used as the cathodic PTL for all of the samples. Platinum-coated bipolar plates with single serpentine flow fields were employed on both sides, that of the cathode also being gold-plated against hydrogen embrittlement. The cells were compressed using polytetrafluoroethylene gaskets with a thickness of 0.3 mm at the cathode and 0.2 mm at the anode, at a torque of 8 N m on each of the eight bolts. The active area was 17.64 cm^2.

Test Equipment and Electrochemical Measurements: All of the single cell experiments were operated using test benches that were developed in-house. High purity feed water (18.2 MΩ cm) was circulated through both the cathode and anode compartments in separate water circuits at a flow rate of 25 mL min^{-1}. All ten water circuits were equipped with compartments that contained ion exchange resin to maintain a high degree of water purity (ASTM Type II). The cells were operated using a DC power supply (TDK Lambda GEN-20-76), which also recorded the current. A multimeter (Keithley Model 2701) was then used to record the voltage. A LabVIEW-based software was utilized to control all devices and record the data. All of the cells were purged with deionized water at 80 °C for 4 h to remove potential ionic impurities prior to installation onto the test bench. For the duration of ≈4000 h, the assembled cells were kept at 80 °C until disassembly and operated at a cell voltage of 2 V, with the exception of some shorter time periods when experimental challenges associated with long-term operation, such as losing supply power, DI water supply, or temperature control had to be managed. Specific cell characteristics and life test conditions are displayed in **Table 2**.

Polarization curves were recorded before and after the durability test using the same equipment. The measurement commenced from open circuit, first increasing the current in 0.025 A cm^{-2} steps to 0.1 A cm^{-2}, and then in 0.2 A cm^{-2} steps until a limiting cell voltage of 2 V was reached. Each step was maintained for 5 min. Electrochemical impedance spectroscopy (EIS) was also conducted before and after the durability test. For these experiments, the cell current was interrupted and the cell connected to a potentiostat (HCP 1005 from Biologic). A DC bias was then applied to the cell using a current perturbation of ±5% of the cell current, with a maximum voltage perturbation of 10 mV and a frequency range of 100 kHz to 100 mHz. The results in this work focused on 1.9 A cm^{-2}.

Contact Resistance: Contact resistance measurements were performed on all samples before and after the durability testing. The PTLs were sandwiched between two conducting, gold-coated plates under a defined compression and probed for their through-plane resistance with a four-wire resistance measurement. The applied contact pressure was varied from 800 to 6000 kPa by an electric press. The sum of the PTL resistance, and the two contact resistances between the sample and gold-coated plates was determined using the applied DC current at 4 A, along with the measured voltage and Ohm's law.

Pinhole: Subsequent to the durability tests, the CCMs were interrogated for failure point development using the ex situ infrared (IR) thermography technique.[43] Nitrogen gas was flowed past the CCM, which was mounted in a sample holder in such a way that the anode was in contact with the nitrogen gas flow and the cathode was in contact with ambient air. The nitrogen was replaced for a short period with a hydrogen pulse. Any hydrogen that permeated or diffused to the cathode would be in contact with oxygen and create an exothermic reaction at the Pt catalyst. The resulting heat signature can be recorded with an IR detector. An apparent local heat signature with a temperature rise of more than 1 °C indicates the loss of membrane integrity at this location. In other words, the technique allows for the detection of pinholes in CCM samples.

Supporting Information

Supporting Information is available from the Wiley Online Library or from the author.

Acknowledgements

The authors would like to thank Hoppe Eugen for the X-ray CT analysis, Dr. Shidong Zhang for the schematic illustration discussion, and Dr. Klaus Wippermann for the impedance discussion. The authors are also grateful to Denise Beate Günther, Daniel Holtz, Stefanie Fischer, and Florian Berg for the experimental support. The authors acknowledge Dr. Simon Geiger for the fruitful discussion. C.L. thanks the China Scholarship Council (CSC) for financial support. This material makes use of the ToF-SIMS system developed at the Colorado School of Mines, which was supported by the National Science Foundation under Grant No. 1726898 and the authors would also like to acknowledge Michael Walker for helpful discussions regarding the ToF-SIMS data. P.P.L. acknowledges support by the Office of Science, Office of Basic Energy Sciences, Materials Sciences and Engineering Division, under Contract No. DE-AC02-06CH11357. This work was authored in part by the National Renewable Energy Laboratory, operated by Alliance for Sustainable Energy, LLC, for the U. S. Department of Energy (DOE) under Contract No. DE-AC36-08GO28308. Funding was provided by the U.S. Department of Energy's Office of Energy Efficiency and Renewable Energy, Hydrogen and Fuel Cell Technologies Office (HFTO). This article has been contributed to by US Government contractors and their work is in the public domain in the USA. The views expressed in the article do not necessarily represent the views of the DOE or the U.S. Government.

Open access funding enabled and organized by Projekt DEAL.

Conflict of Interest

The authors declare no conflict of interest.

Keywords

degradation, durability, iridium, PEM water electrolysis, porous transport layers

Received: September 14, 2020
Revised: December 1, 2020
Published online:

[1] C. Niether, S. Faure, A. Bordet, J. Deseure, M. Chatenet, J. Carrey, B. Chaudret, A. Rouet, *Nat. Energy* **2018**, *3*, 476.
[2] A. Landman, H. Dotan, G. E. Shter, M. Wullenkord, A. Houaijia, A. Maljusch, G. S. Grader, A. Rothschild, *Nat. Mater.* **2017**, *16*, 646.
[3] J. N. Tiwari, S. Sultan, C. W. Myung, T. Yoon, N. Li, M. Ha, A. M. Harzandi, H. J. Park, D. Y. Kim, S. S. Chandrasekaran, W. G. Lee, V. Vij, H. Kang, T. J. Shin, H. S. Shin, G. Lee, Z. Lee, K. S. Kim, *Nat. Energy* **2018**, *3*, 773.
[4] M. Carmo, D. L. Fritz, J. Mergel, D. Stolten, *Int. J. Hydrogen Energy* **2013**, *38*, 4901.
[5] Z. Y. Kang, J. K. Mo, G. Q. Yang, S. T. Retterer, D. A. Cullen, T. J. Toops, J. B. Green, M. M. Mench, F. Y. Zhang, *Energy Environ. Sci.* **2017**, *10*, 166.
[6] K. Ayers, N. Danilovic, R. Ouimet, M. Carmo, B. Pivovar, M. Bornstein, *Annu. Rev. Chem. Biomol. Eng.* **2019**, *10*, 219.
[7] X. Han, Y. Gong, K. K. Fu, X. He, G. T. Hitz, J. Dai, A. Pearse, B. Liu, H. Wang, G. Rubloff, *Nat. Mater.* **2017**, *16*, 572.
[8] K. K. Fu, Y. Gong, B. Liu, Y. Zhu, S. Xu, Y. Yao, W. Luo, C. Wang, S. D. Lacey, J. Dai, *Sci. Adv.* **2017**, *3*, e1601659.
[9] H. Zhang, X. Liao, Y. Guan, Y. Xiang, M. Li, W. Zhang, X. Zhu, H. Ming, L. Lu, J. Qiu, *Nat. Commun.* **2018**, *9*, 3729.
[10] S. Choi, C. J. Kucharczyk, Y. Liang, X. Zhang, I. Takeuchi, H.-I. Ji, S. M. Haile, *Nat. Energy* **2018**, *3*, 202.
[11] N. De Las Heras, E. Roberts, R. Langton, D. Hodgson, *Energy Environ. Sci.* **2009**, *2*, 206.
[12] E. Cho, U.-S. Jeon, H. Ha, S.-A. Hong, I.-H. Oh, *J. Power Sources* **2004**, *125*, 178.
[13] A. Ingenito, G. Nogay, Q. Jeangros, E. Rucavado, C. Allebé, S. Eswara, N. Valle, T. Wirtz, J. Horzel, T. Koida, *Nat. Energy* **2018**, *3*, 800.
[14] T. G. Allen, J. Bullock, X. Yang, A. Javey, S. De Wolf, *Nat. Energy* **2019**, *4*, 914.
[15] M. Bühler, F. Hegge, P. Holzapfel, M. Bierling, M. Suermann, S. Vierrath, S. Thiele, *J. Mater. Chem. A* **2019**, *7*, 26984.
[16] P. Lettenmeier, S. Kolb, N. Sata, A. Fallisch, L. Zielke, S. Thiele, A. S. Gago, K. A. Friedrich, *Energy Environ. Sci.* **2017**, *10*, 2521.
[17] T. Schuler, J. M. Ciccone, B. Krentscher, F. Marone, C. Peter, T. J. Schmidt, F. N. Büchi, *Adv. Energy Mater.* **2020**, *10*, 1903216.
[18] J. R. Miller, R. Outlaw, B. Holloway, *Science* **2010**, *329*, 1637.
[19] L. Zheng, Y. Xu, D. Jin, Y. Xie, *J. Mater. Chem.* **2010**, *20*, 7135.
[20] C. Lei, F. Markoulidis, Z. Ashitaka, C. Lekakou, *Electrochim. Acta* **2013**, *92*, 183.
[21] C. Liu, M. Carmo, G. Bender, A. Everwand, T. Lickert, J. L. Young, T. Smolinka, D. Stolten, W. Lehnert, *Electrochem. Commun.* **2018**, *97*, 96.
[22] Z. Y. Kang, J. K. Mo, G. Q. Yang, Y. F. Li, D. A. Talley, S. T. Retterer, D. A. Cullen, T. J. Toops, M. P. Brady, G. Bender, B. S. Pivovar, J. B. Green, F. Y. Zhang, *Appl. Energy* **2017**, *206*, 983.
[23] C. Rakousky, U. Reimer, K. Wippermann, M. Carmo, W. Lueke, D. Stolten, *J. Power Sources* **2016**, *326*, 120.
[24] C. Rakousky, G. P. Keeley, K. Wippermann, M. Carmo, D. Stolten, *Electrochim. Acta* **2018**, *278*, 324.
[25] H. Y. Jung, S. Y. Huang, P. Ganesan, B. N. Popov, *J. Power Sources* **2009**, *194*, 972.
[26] H. Y. Jung, S. Y. Huang, B. N. Popov, *J. Power Sources* **2010**, *195*, 1950.
[27] A. S. Gago, S. A. Ansar, B. Saruhan, U. Schulz, P. Lettenmeier, N. A. Canas, P. Gazdzicki, T. Morawietz, R. Hiesgen, J. Arnold, K. A. Friedrich, *J. Power Sources* **2016**, *307*, 815.
[28] P. Lettenmeier, R. Wang, R. Abouatallah, F. Burggraf, A. S. Gago, K. A. Friedrich, *J. Electrochem. Soc.* **2016**, *163*, F3119.
[29] G. Q. Yang, S. L. Yu, J. K. Mo, Z. Y. Kang, Y. Dohrmann, F. A. List, J. B. Green, S. S. Babu, F. Y. Zhang, *J. Power Sources* **2018**, *396*, 590.
[30] D. M. Brunette, P. Tengvall, M. Textor, P. Thomsen, *Titanium in Medicine: Material Science, Surface Science, Engineering, Biological Responses and Medical Applications*, Springer Science & Business Media, Berlin **2012**.
[31] S. M. Alia, S. Stariha, R. L. Borup, *J. Electrochem. Soc.* **2019**, *166*, F1164.
[32] K. Ayers, Information obtained via E-Mail exchange with K. Ayers—NEL on the 28 Nov. **2019**.
[33] P. Millet, S. Grigoriev, in *Renewable Hydrogen Technologies: Production, Purification, Storage, Applications and Safety*, (Eds: L. M. Gandia, G. Arzamendi, M. Diéguez), Elsevier, Amsterdam, The Netherlands **2013**, p. 19.
[34] S. Cherevko, S. Geiger, O. Kasian, A. Mingers, K. J. Mayrhofer, *J. Electroanal. Chem.* **2016**, *773*, 69.
[35] S. M. Alia, B. Rasimick, C. Ngo, K. C. Neyerlin, S. S. Kocha, S. Pylypenko, H. Xu, B. S. Pivovar, *J. Electrochem. Soc.* **2016**, *163*, F3105.
[36] S. Siracusano, V. Baglio, S. A. Grigoriev, L. Merlo, V. N. Fateev, A. S. Arico, *J. Power Sources* **2017**, *366*, 105.
[37] Y. T. Kim, P. P. Lopes, S. A. Park, A. Y. Lee, J. Lim, H. Lee, S. Back, Y. Jung, N. Danilovic, V. Stamenkovic, J. Erlebacher, J. Snyder, N. M. Markovic, *Nat. Commun.* **2017**, *8*, 1449.
[38] N. Danilovic, R. Subbaraman, K.-C. Chang, S. H. Chang, Y. J. Kang, J. Snyder, A. P. Paulikas, D. Strmcnik, Y.-T. Kim, D. Myers, *J. Phys. Chem. Lett.* **2014**, *5*, 2474.
[39] https://en.wikipedia.org/wiki/List_of_thermal_conductivities (accessed: December 2020).
[40] P. Lettenmeier, J. Majchel, L. Wang, V. A. Saveleva, S. Zafeiratos, E. R. Savinova, J. J. Gallet, F. Bournel, A. S. Gago, K. A. Friedrich, *Chem. Sci.* **2018**, *9*, 3570.
[41] V. A. Saveleva, L. Wang, D. Teschner, T. Jones, A. S. Gago, K. A. Friedrich, S. Zafeiratos, R. Schlogl, E. R. Savinova, *J. Phys. Chem. Lett.* **2018**, *9*, 3154.
[42] L. P. Buchwalter, *J. Adhes. Sci. Technol.* **1987**, *1*, 341.
[43] M. Ulsh, A. DeBari, J. M. Berliner, I. V. Zenyuk, P. Rupnowski, L. Matvichuk, A. Z. Weber, G. Bender, *Int. J. Hydrogen Energy* **2019**, *44*, 8533.
[44] M. Kruth, D. Meertens, K. Tillmann, *J. Large-Scale Res. Facil.* **2016**, *2*, 59.
[45] A. Kovács, R. Schierholz, K. Tillmann, *J. Large-Scale Res. Facil.* **2016**, *2*, 43.
[46] L. Wang, P. Lettenmeier, U. Golla-Schindler, P. Gazdzicki, N. A. Cañas, T. Morawietz, R. Hiesgen, S. S. Hosseiny, A. S. Gago, K. A. Friedrich, *Phys. Chem. Chem. Phys.* **2016**, *18*, 4487.